Enormous electron-electron scattering in the filled-cage cubic compound $Ba_{10}Ti_{24}Bi_{39}$

Fei Han,[1,2] Jin-Ke Bao,[1] Christos D. Malliakas,[1,3] Mihai Sturza,[1,4] Yongping Du,[5] Duck Young Chung,[1] Xiangang Wan,[5] and Mercouri G. Kanatzidis[1,3,*]

[1]*Materials Science Division, Argonne National Laboratory, Argonne, Illinois 60439, USA*

[2]*Department of Nuclear Science and Engineering, Massachusetts Institute of Technology, Cambridge, Massachusetts 02139, USA*

[3]*Department of Chemistry, Northwestern University, Evanston, Illinois 60208, USA*

[4]*Leibniz Institute for Solid State and Materials Research Dresden IFW, Institute for Solid State Research, 01069 Dresden, Germany*

[5]*National Laboratory of Solid State Microstructures, School of Physics, Collaborative Innovation Center of Advanced Microstructures, Nanjing University, Nanjing 210093, China*

(Received 8 June 2019; revised manuscript received 25 August 2019; published 7 October 2019)

The cubic intermetallic compound $Ba_{10}Ti_{24}Bi_{39}$ has a Ba_6Bi_{16} polyhedral cage with a Bi guest atom encapsulated inside. The compound can be formulated as $Ba_5Ti_{12}Bi_{19+x}$ when x signifies the extra Bi atoms filling cages. It crystallizes in a complex noncentrosymmetric cubic structure in space group P-43m with cell parameter $a = 12.6787(4)$ Å. The guest Bi atoms distribute diffusely in the cages and seem to play a role in stabilizing the crystal structure. The magnetic susceptibility of this compound shows a weak temperature dependence with a positive slope coefficient. The charge transport properties as a function of temperature exhibit two competing components which are in charge of positive and negative magnetoresistances. Electronic band-structure calculations reveal the complex multiband hybridization of Ti/Bi orbitals near the Fermi surface, which may play a role in the enormous electron-electron scattering in this material evidenced by the large Kadowaki-Woods ratio.

DOI: 10.1103/PhysRevMaterials.3.105001

I. INTRODUCTION

Bismuth is unique among metallic elements as it is located closest to the border of metal and semiconductor, possesses the largest degree of spin-orbit coupling, and has the smallest Fermi surface among all the nonradioactive elements. When bismuth forms intermetallics, it can adopt bonding that spans the entire spectrum between metallic and ionic. The variety of the bonding characters in bismuthides results in electronic properties of semiconductor to semimetal to metal. Furthermore, the strong spin-orbit coupling (SOC) effects can cause splitting of electronic bands giving rise to topologically nontrivial electronic structures [1,2]. During the past several years, several novel phenomena have been reported in bismuthides, including superconductivity in $NiBi_3$ [3], $Ca_{11}Bi_{10-x}$ [4], NaBi [5], and $BaBi_3$ [6]; Dirac fermions in Na_3Bi [7–9], $AeMnBi_2$ (Ae = Ca, Sr, Ba) [10–14], and $LaAgBi_2$ [15]; possible topological superconductivity in β-$PdBi_2$ [16] and RPdBi (R = rare earth) [17]; and topological semimetallicity and large magnetoresistance (MR) in LaBi [18–20]. These discoveries motivate the further exploration of new phases. Some new compounds such as the superconductors $CoBi_3$ [21], $Cu_{11}Bi_7$ [22], and $LaPd_{1-x}Bi_2$ [23,24], the antiferromagnetic Kondo lattice compound $CePd_{1-x}Bi_2$ [25], their analogs $RNi_{1-x}Bi_{2\pm y}$ (R = La-Nd, Sm, Gd-Dy) [26] and $RAuBi_2$ (R = La-Nd, Sm, Gd) [27,28], and the first iron-bismuth bonding material $FeBi_2$ [29] are notable examples. Recently, the synthesis and characterization of $Ba_{10}Ti_{24}Bi_{39}$ was reported to form from Bi flux [30].

In this work we investigate this unusual ternary bismuthide $Ba_{10}Ti_{24}Bi_{39}$. The formulation $(Ba^{2+})_{10}(Ti^{4+})_{24}(Bi^{3-})_{39}$ is almost electronically charge balanced, suggesting $Ba_{10}Ti_{24}Bi_{39}$ is possibly a Zintl phase [31]. $Ba_{10}Ti_{24}Bi_{39}$ adopts a novel filled-cage structure with a disordered guest encapsulated in the cage [30]. We report here that this compound displays a two-component behavior in magnetoresistance, and an enormous degree of electron-electron scattering in its electronic transport.

II. EXPERIMENTAL SECTION

A. Sample preparation

We grew the $Ba_{10}Ti_{24}Bi_{39}$ crystals from Bi flux. An approximate total of 3 g of Ba ingot, Ti powder, and Bi granules in the molar ratio of 5:12:100 was mixed and loaded in an alumina crucible. The handling of chemicals was performed in a glovebox with an argon atmosphere (both H_2O and O_2 are limited below 0.1 ppm). The alumina crucible with its opening covered by a stainless steel sieve was sealed in an evacuated silica tube. The silica tube was heated to 900 °C in a box furnace and kept at 900 °C for 24 h. Then a slow-cooling process from 900 to 400 °C was carried out during 100 h. At 400 °C the excess Bi flux was canted by centrifugation. Polyhedral crystals with metallic luster [as shown in Fig. 1(a)] were collected on the stainless steel sieve. The obtained air-sensitive crystals had a typical dimension of $2\times2\times2$ mm^3. The yield was near 50% based on the amount of Ba and Ti. Due to the possible reaction between Ti metal and alumina

*Corresponding author: m-kanatzidis@northwestern.edu

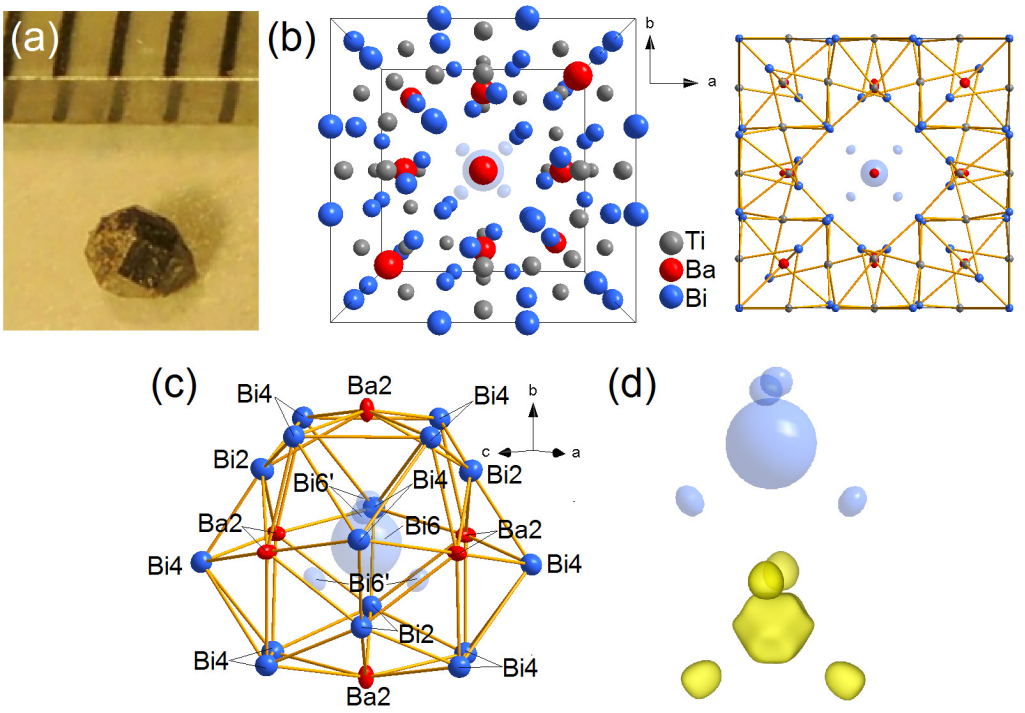

FIG. 1. (a) Photograph of a typical $Ba_{10}Ti_{24}Bi_{39}$ crystal. (b) Crystal structure of $Ba_{10}Ti_{24}Bi_{39}$. (c) Cagelike structure composed of Ba(2), Bi(2), and Bi(4) atoms with one Bi(6) atom encapsulated inside. (d) Ellipsoid representation of Bi(6) and Bi(6)′ (top), and the electron density distribution generated by Fourier transform from the single-crystal diffraction data (bottom).

crucible [32], we also grew the $Ba_{10}Ti_{24}Bi_{39}$ single crystals by directly loading the mixture into the silica tube. The results of those two methods are similar to each other except that we got a minor phase ε-TiO [33] with a needle shape when the alumina crucible for crystal growth was used [see Fig. S5 in Supplemental Material (SM)] [34]. To avoid possible interference of the residual Bi flux on property measurements, the crystals were cleaved with a blade inside a glovebox and only the inner parts of the crystals were used for structural and physical property characterization.

B. Single-crystal x-ray diffraction

A piece of well-formed crystal was picked out with the help of an optical microscope located in the glovebox. The crystal was fixed in a glass capillary with Dow Corning high vacuum grease. Then the capillary was evacuated and flame sealed to keep the crystal stable. Single-crystal x-ray-diffraction measurement was done on a STOE IPDS-2T diffractometer at room temperature. Data reduction, integration, and absorption correction were performed with the software X-Area [35], and the structure was solved by the direct methods and refined using the SHELXTL software [36]. The resulting structure parameters are listed in Tables I and II below and Table S1 in SM [34].

C. Magnetization measurements

Magnetization measurements for $Ba_{10}Ti_{24}Bi_{39}$ were carried out on a commercial Quantum Design magnetic property measurement system (MPMS3). A crystal (sample Q1) of 90.6 mg selected from the batch which was grown in a silica tube was directly mounted on a quartz sample holder with a negligible amount of GE varnish. The data presented in the main text are from the sample Q1. Another crystal (sample A1) of 66.3 mg grown in the alumina crucible were also checked for its magnetic properties, whose results were presented in SM [34].

D. Resistivity and magnetoresistance measurements

After the crystals were cleaved in the glovebox, a piece of bar-shaped crystal with a clean surface was selected for resistivity and magnetoresistance measurements. The measurements were carried out on a Quantum Design physical property measurement system (PPMS) with magnetic fields up to 9 T. The contacts in four-probe geometry were made with gold wires and silver paint under the protection of the glovebox. For the magnetoresistance measurements, the field was applied approximately perpendicular to the longitudinal dimension of the crystal.

E. Specific-heat measurements

We employed the thermal relaxation technique to perform the specific-heat measurement on the Quantum Design PPMS. N-grease was used as heat-conducting medium.

F. Band-structure calculations

Band-structure calculations for $Ba_{10}Ti_{24}Bi_{39}$ were performed with the Vienna *ab initio* simulation package [37,38]. The results were obtained by using the generalized gradient

TABLE I. Crystal data and structure refinement for $Ba_{10}Ti_{24}Bi_{39}$ at 293(2) K.

Parameter	Value
Empirical formula	$Ba_{10}Ti_{24}Bi_{39}$
Formula weight	10 673.22 g/mol
Temperature	293(2) K
Wavelength	0.71073 Å
Crystal system	Cubic
Space group	*P*-43*m*
Unit-cell dimensions	$a = 12.6787(4)$ Å, $\alpha = 90.00^\circ$ $b = 12.6787(4)$ Å, $\beta = 90.00^\circ$ $c = 12.6787(4)$ Å, $\gamma = 90.00^\circ$
Volume	2038.09(11) $Å^3$
Z	1
Density (calculated)	8.696 g/cm^3
Absorption coefficient	90.739 mm^{-1}
F(000)	4325
Crystal size	$0.1\times0.1\times0.1$ mm^3
θ range for data collection	2.78 to 24.98°
Index ranges	$-15 \leqslant h \leqslant 15$, $-15 \leqslant k \leqslant 15$, $-15 \leqslant l \leqslant 15$
Reflections collected	13 043
Independent reflections	732 ($R_{int} = 0.0562$)
Completeness to $\theta = 24.98^\circ$	99.5%
Refinement method	Full-matrix least squares on F^2
Data, restraints, and parameters	732, 0, and 47
Goodness of fit	1.226
Final *R* indices [$> 2\sigma(I)$]	R_{obs}[a] = 0.0289, wR_{obs}[a] = 0.0577
R indices (all data)	R_{all}[a] = 0.0311, wR_{all}[a] = 0.0584
Largest diffraction peak and hole	2.548 and −3.545 e $Å^{-3}$

[a]$R = \Sigma||F_o|-|F_c||/\Sigma|F_o|$, $wR = \{\Sigma[w(|F_o|^2 - |F_c|^2)^2]/\Sigma[w(|F_o|^4)]\}^{1/2}$ and calc $w = 1/[\sigma^2(F_o^2) + (0.0324P)^2 + 0.2990P]$ where $P = (F_o^2 + 2F_c^2)/3$.

approximation (GGA) Perdew-Burke-Ernzerhof function [39]. An energy cutoff of 400 eV was adopted for the plane-wave expansion of the electronic wave function and the energy convergence criterion was set to 10^{-5} eV. To sample the Brillouin zone, appropriate k-point meshes of (9×9×9) were used for calculations. The SOC effect was taken into account by the second variation method [40].

TABLE II. Atomic coordinates ($\times10^4$) and equivalent isotropic displacement parameters ($Å^2\times10^3$) for $Ba_{10}Ti_{24}Bi_{39}$ at 293(2) K with estimated standard deviations in parentheses.

Label	*x*	*y*	*z*	Occupancy	U_{eq}[a]
Ti(1)	1608(3)	1608(3)	3285(4)	1	18(1)
Ti(2)	1827(3)	5000	0	1	16(1)
Ba(1)	8356(2)	8356(2)	8356(2)	1	26(1)
Ba(2)	1766(2)	5000	5000	1	36(1)
Bi(1)	3342(1)	3342(1)	120(1)	1	17(1)
Bi(2)	3225(1)	3225(1)	3225(1)	1	20(1)
Bi(3)	3560(1)	0	0	1	16(1)
Bi(4)	2194(1)	2194(1)	5478(1)	1	19(1)
Bi(5)	1113(1)	1113(1)	1113(1)	1	19(1)
Bi(6)	5000	5000	5000	0.70(3)	191(12)
Bi(6′)	5878(9)	4122(9)	4122(9)	0.074(7)	22(7)

[a]U_{eq} is defined as one-third of the trace of the orthogonalized U_{ij} tensor.

III. RESULTS AND DISCUSSION

A. Crystal structure

$Ba_{10}Ti_{24}Bi_{39}$ (also formulated as $Ba_5Ti_{12}Bi_{19+x}$) crystallizes in a complex noncentrosymmetric cubic structure in space group *P*-43*m* with cell parameter $a = 12.6787(4)$ Å. The structure of $Ba_{10}Ti_{24}Bi_{39}$ solved by our single-crystal crystallographic study and projected along the *c* axis is depicted in Fig. 1(b). This structure is very similar to that of $Ba_5Ti_{12}Sb_{19+x}$ ($x \leqslant 0.2$) reported earlier since $Ba_5Ti_{12}Sb_{19+x}$ ($x \leqslant 0.2$) can also be denoted by $Ba_{10}Ti_{24}Sb_{38+x}$ ($x \leqslant 0.4$) [41]. The atomic positions and the occupancies of most atoms, excluding the variable-amount Bi/Sb atom, in the two materials are almost the same. In the center of the cubic unit cell of $Ba_{10}Ti_{24}Bi_{39}$, six Ba(2) atoms, four Bi(2) atoms, and 12 Bi(4) atoms form a cagelike structure which has one Bi(6) atom encapsulated inside, as shown in Fig. 1(c). The distances from the center of the cage to the Ba(2), Bi(2), and Bi(4) atoms are 4.100(3), 3.8984(10), and 5.0686(7) Å, respectively. These are longer than the regular Ba-Bi and Bi-Bi bonding distances, so the Bi(6) atom is not stable sitting precisely at the center position. Instead, Bi(6) adopts a positional disorder, similar to disordered guests in cagelike structures of hydrogen clathrate hydrates and some inorganic clathrates [42,43]. Specific to $Ba_{10}Ti_{24}Bi_{39}$, the Bi(6) site splits into Bi(6) and Bi(6)′ and the displacement factors of the Bi(6) site are relatively large, as exhibited in the ellipsoid model in the top panel of Fig. 1(d).

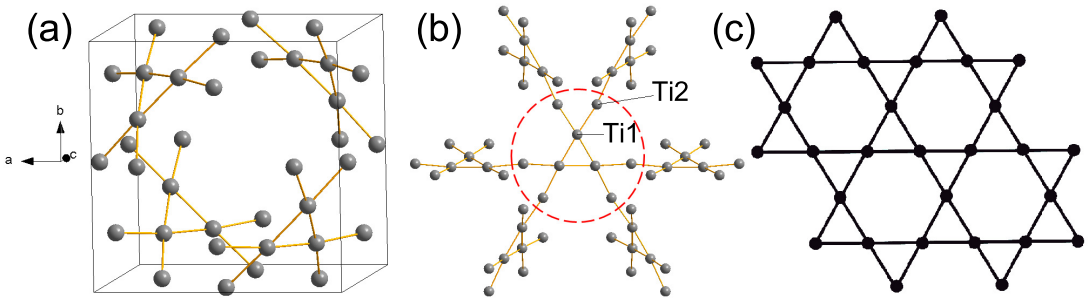

FIG. 2. (a) Ti sublattice in the structure of $Ba_{10}Ti_{24}Bi_{39}$. (b) Kagome-lattice-like structure fragment (in the red circle) in the Ti sublattice of $Ba_{10}Ti_{24}Bi_{39}$ and how they connect. (c) Classic Kagome lattice.

The electron-density distribution generated by Fourier transform from the single-crystal diffraction data is presented in the bottom panel of Fig. 1(d) reflecting the real-space distribution of the Bi(6) atoms. The total number of Bi(6) atoms in one unit cell based on the occupancy of Bi(6) and Bi(6)′ is 1, suggesting that all the cages in the structure of $Ba_{10}Ti_{24}Bi_{39}$ are filled. The differences between the structures of $Ba_{10}Ti_{24}Bi_{39}$ and $Ba_5Ti_{12}Sb_{19+x}$ are mainly on features of guest atoms. Unlike the split position, the disordered distribution, and the 100% occupancy of Bi(6) guest atoms in $Ba_{10}Ti_{24}Bi_{39}$, only a few of the cages in $Ba_5Ti_{12}Sb_{19+x}$ are filled by guest atoms, and in the filled cages the Sb(6) guest atoms occupy only the site (0.6354(5), 0.6354(5), 0.6354(5)) locally [41], a site like Bi(6)' but closer to the facets of the polyhedral cage. This indicates the significantly smaller cage in $Ba_5Ti_{12}Sb_{19+x}$ can be self-stabilizing without guest atoms.

A striking feature of $Ba_{10}Ti_{24}Bi_{39}$ is the Ti sublattice which is built up of a three-dimensional network of intersecting Kagome-lattice-like structure fragments [see Fig. 2(a)]. As shown in Fig. 2(b), the fragment units (indicated in the red circle) connect to each other by sharing Ti(2) atoms to form an infinite three-dimensional network. It is known that Kagome-lattice-type configuration of magnetic atoms, as shown in Fig. 2(c), will lead to magnetic frustration or multiple competing magnetic interactions in the lattice [44]. The three-dimensional network of intersecting Kagome-lattice-like fragments in $Ba_{10}Ti_{24}Bi_{39}$ may also bring on unusual magnetic properties in this material as we discuss below.

B. Magnetic properties

Magnetic susceptibility of $Ba_{10}Ti_{24}Bi_{39}$ shows a very weak temperature dependence (see Fig. 3). The magnetizations versus fields at different temperatures are almost linear up to 7 T as shown in the inset of Fig. 3. There is a tiny magnetic hysteresis loop at low magnetic fields at 10 K, indicating a very small amount of ferromagnetic impurities in the sample (see Fig. S4 in SM [34]). However, this will not affect the magnetic susceptibility data measured at high magnetic fields ($\mu_0 H = 5$ T). The upturn below 14 K is probably due to paramagnetic impurities or defects in the sample. It does not show a Curie-Weiss law from 15 to 300 K. The almost linear temperature-dependent magnetic susceptibility with a positive slope in $Ba_{10}Ti_{24}Bi_{39}$, possibly originating from the three-dimensional network of intersecting Kagome-lattice-like fragments in $Ba_{10}Ti_{24}Bi_{39}$, is similar to the cases in the high-temperature iron-based superconducting parent compounds which are believed to be due to antiferromagnetic fluctuations above the spin-density wave transition in those compounds [45]. However, there is no magnetic order detected in $Ba_{10}Ti_{24}Bi_{39}$ below room temperature. The relative change in magnetic susceptibility from 300 to 50 K in $Ba_{10}Ti_{24}Bi_{39}$ is only 12%, which can also be interpreted by a dominant temperature-independent Pauli paramagnetism of the sample supported by density functional theory calculations shown below with some unknown antiferromagnetic contributions. We have also performed magnetic susceptibility measurements on another crystal (sample A1) grown under a different condition, the result of which shows exactly the same temperature-dependent behavior (see the data in SM [34]). The origin of the almost linear temperature-dependent magnetic susceptibility in $Ba_{10}Ti_{24}Bi_{39}$ is unclear and likely due to the unusual magnetic interaction in the three-dimensional network of intersecting Kagome-lattice-like fragments. Further investigations will be needed to elucidate this issue, which is outside the scope of this paper.

C. Resistivity and magnetoresistance

The electrical resistivity for $Ba_{10}Ti_{24}Bi_{39}$ as a function of temperature is displayed in the main frame of Fig. 4(a). The

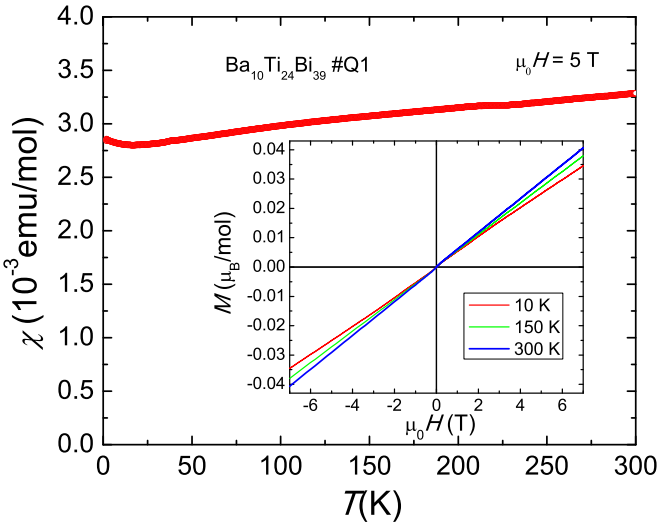

FIG. 3. (a) Temperature dependences of magnetic susceptibility measured at $\mu_0 H = 5$ T for single-crystalline $Ba_{10}Ti_{24}Bi_{39}$ sample Q1. Inset: Isothermal magnetizations at 10, 150, and 300 K.

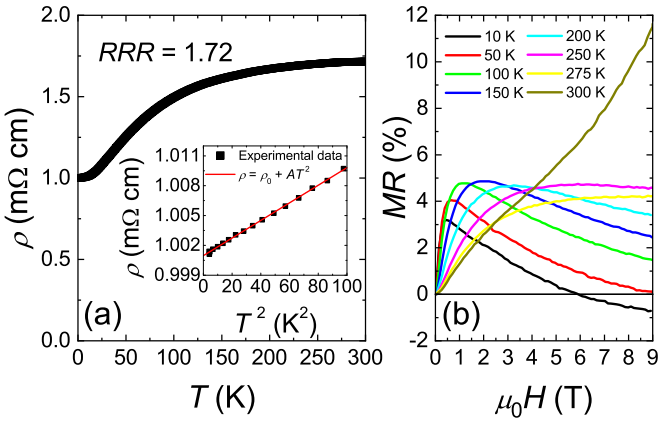

FIG. 4. (a) Temperature dependence of resistivity for $Ba_{10}Ti_{24}Bi_{39}$. Inset: Power-law fitting to the low-temperature part of resistivity. (b) Field dependence of magnetoresistance (MR) at different temperatures for $Ba_{10}Ti_{24}Bi_{39}$. At 10 K the MR undergoes a positive-to-negative sign reversal.

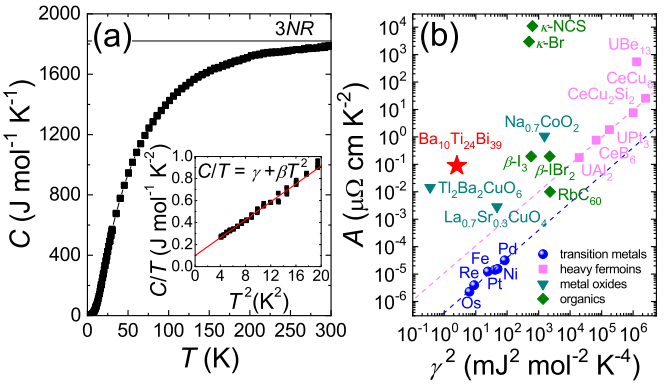

FIG. 5. (a) Temperature dependence of specific heat for $Ba_{10}Ti_{24}Bi_{39}$. Inset: Specific heat divided by temperature C/T as a function of T^2. The red line shows a linear fit to the low-temperature part of the C/T vs T^2 curve. The slope and intercept of the red line represent β and γ, respectively. (c) The standard Kadowaki-Woods plot. In labeling the data points we use the following abbreviations: κ-Br is κ-(BEDT-TTF)$_2$Cu [N(CN)$_2$]Br; κ-NCS is κ-(BEDT-TTF)$_2$Cu(NCS)$_2$; β-I$_3$ is β-(BEDT-TTF)$_2$I$_3$; and β-IBr$_2$ is β-(BEDT-TTF)$_2$IBr$_2$.

resistivity has a high residual value ρ_0 at 2 K and the residual resistivity ratio was calculated to be 1.72, which is very small for a single-crystal sample. This reflects an extremely strong transport scattering in this material. The strong charge transport scattering can be attributed to the complexity of disorder in the structure, particularly the disorder of the guest atoms. Above 25 K, the resistivity shows an unconventional bow-shaped behavior. This kind of behavior was found in many strongly correlated systems, for instance, in $Rh_{17}S_{15}$ [46], κ-(BEDT-TTF)$_2$Cu [N(CN)$_2$]Br [47], and LiV_2O_4 [48].

We observed a T^2 temperature dependence for the low-temperature part of the resistivity, $\rho(T) = \rho_0 + AT^2$, establishing the existence of a well-defined Fermi-liquid state at low temperatures, as shown in the inset of Fig. 4(a). From the linear fitting process we obtain $\rho_0 = 1.000\,\mathrm{m\Omega\,cm}$ and $A = 0.0885\,\mu\Omega\,\mathrm{cm/K^2}$. The coefficient A for this material is significantly larger than that of simple metals, which is typically around $10^{-5}\,\mu\Omega\,\mathrm{cm/K^2}$. The significantly enhanced A greatly increases the contribution of the T^2 term to the resistivity, which causes a fast upturn with the increase of temperature in the low-temperature resistivity of $Ba_{10}Ti_{24}Bi_{39}$. This is sharply contrasted to the case of simple metals where the resistivity has a flat low-temperature part. As the T^2 term arises from the electron-electron scattering, the $Ba_{10}Ti_{24}Bi_{39}$ appears to exhibit very large electron-electron scattering below 10 K in its electronic transport.

We used MR measurements as a tool for investigating the properties of electronic scattering [49,50]. Field dependences of magnetoresistance at different temperatures for $Ba_{10}Ti_{24}Bi_{39}$ are shown in Fig. 4(b). We find the magnetoresistance significantly varies with temperature and magnetic field. At 300 K the magnetoresistance rises steadily with magnetic field with no signs of saturation. However, at 275 K the magnetoresistance rises from 0 to 5 T but then saturates above 5 T. At lower temperatures the magnetoresistance rises first and then undergoes a broad maximum at moderate fields followed by a falling at higher fields. At 10 K it reaches a broad maximum at very low field and then decreases quickly; at 6 T the magnetoresistance drops to zero and has a sign reversal from positive to negative. A similar MR behavior was also observed in other crystals from the same batch (see Fig. S9 in SM [34]). We suggest the magnetoresistance behavior can be explained with a mixture of two competing components, one positive and the other negative. At low temperatures the contributions of the two components are comparable while at high temperatures the positive component dominates and the negative component is diminished. The negative MR component is probably due to weak localization [51] from the significant disorder in this material as proven above. The relative contributions of positive and negative components in MR vary in different crystals due to the possibly different defect distributions in those crystals.

D. Specific heat

Specific-heat measurements for $Ba_{10}Ti_{24}Bi_{39}$ were performed from 2 to 300 K [see Fig. 5(a)]. No peaks or jumps associated with structural or magnetic transitions were observed. At 300 K, the specific heat approaches the value of $3NR$, the so-called Dulong-Petit limit, where $N = 73$ (the number of atoms in the chemical formula) and $R = 8.314\,\mathrm{J\,mol^{-1}\,K^{-1}}$ (the gas constant). This is consistent with the stoichiometry and suggests there are no massive vacancies in the structure. As predicted by Fermi-liquid theory, at very low temperatures, the specific heat C is approximate to the sum of the first term of phonon specific heat βT^3 and the first term of electronic specific heat γT. In other words, the C/T versus T^2 curve follows a linear relationship $C/T = \gamma + \beta T^2$ at low temperatures, as shown in the inset of Fig. 2(b). From linear fitting, we can estimate the electronic specific-heat coefficient γ to be $100.2\,\mathrm{mJ\,mol^{-1}\,K^{-2}}$ and the phonon specific heat coefficient β to be $40.73\,\mathrm{mJ\,mol^{-1}\,K^{-4}}$.

Taking the value of β into the formula $\theta_D = (12\pi^4 NR/5\beta)^{1/3}$, we obtain a Debye temperature θ_D of 151.6 K for $Ba_{10}Ti_{24}Bi_{39}$ which is very close to those of other bismuth-rich compounds. According to the band-structure

calculations to be discussed in the next subsection, the conductive electrons in this system are provided by all the Ti and Bi atoms. Therefore, we can distribute the value of γ to each Ti or Bi atom, so that γ equals 1.590 mJ mol^{-1} K^{-2} for per mole Ti or Bi atoms. Using the coefficient A obtained in the fitting of the resistivity, we can calculate the Kadowaki-Woods ratio A/γ^2, which is the criterion for the strength of electron-electron scattering [52], for the present material to be 35 $\mu\Omega$ cm mol^2 K^2 J^{-2}.

For simple metals the ratio A/γ^2 is typically a constant [53], while it is significantly enhanced for heavy-fermion materials, which was first raised by Kadowaki and Woods [52]. The A/γ^2 has become known as the Kadowaki-Woods ratio and its magnitude is regarded as a measure for the strength of electron-electron scattering in materials [54,55].

To compare the Kadowaki-Woods ratio for $Ba_{10}Ti_{24}Bi_{39}$ with other materials, we add the data of $Ba_{10}Ti_{24}Bi_{39}$ into the standard Kadowaki-Woods plot [see Fig. 5(b)]. This plot was introduced in Ref. [56] and contains data for different transition metals, heavy-fermion materials, and other systems with a large Kadowaki-Woods ratio. From Fig. 5(b), we can see the data for the transition metals and the heavy-fermion materials, respectively, fall on two separate lines, which represents the universal relationships of the Kadowaki-Woods ratio for simple metals and heavy-fermion materials. The point for $Ba_{10}Ti_{24}Bi_{39}$ is located well above the two lines, indicating the Kadowaki-Woods ratio for this compound is very large. From the data presented in the standard Kadowaki-Woods plot [56], we find the Kadowaki-Woods ratio for $Ba_{10}Ti_{24}Bi_{39}$ is among the largest values observed in materials.

The giant Kadowaki-Woods ratio reveals the electron-electron scattering in $Ba_{10}Ti_{24}Bi_{39}$ is enormous. Different from the case in the heavy-fermion materials, the enormous electron-electron scattering in $Ba_{10}Ti_{24}Bi_{39}$ does not have f electrons and no Kondo physics is involved. This possibly suggests an unprecedented origin for the enormous electron-electron scattering in intermetallics.

E. Band structure

To better understand the magnetic and electronic properties of $Ba_{10}Ti_{24}Bi_{39}$, we calculated the electronic band structure using first-principles density functional theory. As shown in Fig. 6(a), there are several bands crossing the Fermi energy making the system a metal, which is consistent with the experimental results.

When the large SOC effect of Bi atoms is taken into account the electronic structure of $Ba_{10}Ti_{24}Bi_{39}$ is shown in Fig. 6(b). Comparing with the band structure without considering SOC, the bands near the Fermi energy are split by the SOC effect. After the band splitting, more bands cross the Fermi level and lead to a more complicated band structure, which indicates the SOC effect cannot be neglected in this compound. The SOC effect kills the hole pocket at the Γ point and brings up more small Fermi pockets. The system is still a metal after considering SOC because several bands cross the Fermi level. The bands near the Fermi energy are split by the SOC effect and hybridize again, thus forming a very complicated Fermi surface. From Fig. 6(b), we can see that a few electron and hole pockets coexist. The electronic specific-

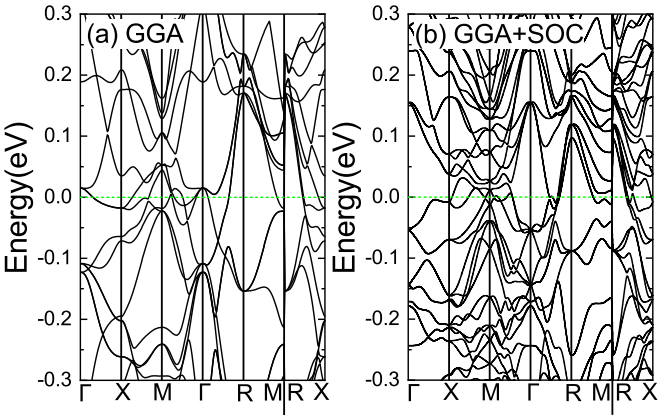

FIG. 6. Band structures along the high-symmetry points in the reduced Brillouin zone calculated by GGA (a) without and (b) with considering SOC. The horizontal green dashed lines refer to the Fermi energy level.

heat coefficient γ is calculated to be 194 mJ mol^{-1} K^{-2}, which is consistent with the experimental one.

As shown in Fig. 7(a), there is a peak in the density of states (DOS) at the Fermi level when SOC is not considered. This suggests the possibility of Stoner instability [57] against ferromagnetism (FM). However, after performing a spin-polarized calculation using GGA+SOC with initial FM setup we found that it converges to a non-magnetic-order ground state. The peak at the Fermi level is also removed after turning on SOC for the calculations [see Fig. 7(b)].

Figures 7(b) and 7(c) present the total and atomic DOS when SOC is considered. We can see all the Bi and Ti atoms contribute to the total DOS of the system. Compared with the Bi-6p electrons, the Ti-3d electrons are more dominated. However, differently from other Bi atoms, the Bi(6) atom in the cage gives the highest DOS at the Fermi level among all atoms. We suggest the enormous electron-electron scattering

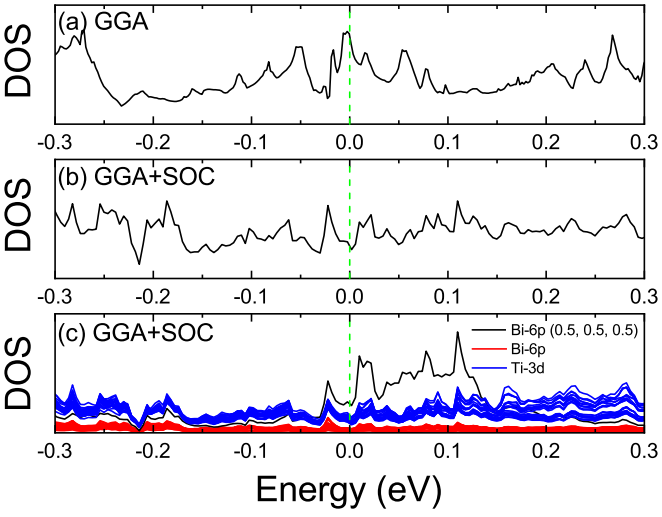

FIG. 7. (a) Total density of states (DOS) at around the Fermi energy level without SOC considered. (b) Total DOS with SOC considered. (c) Atomic orbital projected DOS with SOC considered. The vertical green dashed lines refer to the Fermi energy level.

in $Ba_{10}Ti_{24}Bi_{39}$ arises from the complex multiband hybridization near the Fermi surface. The random distribution of the Bi(6) atom may play an important role since the Bi(6) atom gives the highest proportion in the DOS at the Fermi level.

IV. CONCLUSIONS

The cubic noncentrosymmetric compound $Ba_{10}Ti_{24}Bi_{39}$ has a filled-cage structure with guest atoms distributing randomly in the cages. It shows a positive temperature-dependent coefficient in the magnetic susceptibility, the origin of which needs further investigations. The magnetoresistance at low temperatures has a positive to negative crossover with increasing the magnetic fields, indicating two competing factors in determining the transport properties. The complex multiband hybridization of the abundance of Ti and Bi atoms near the Fermi surface may play a role in the enormous electron-electron scattering in this material, which is revealed by the large Kadowaki-Woods ratio among the top ones for intermetallics.

ACKNOWLEDGMENTS

We thank Dr. Daniel Phelan for help with the magnetic susceptibility measurements. This work was supported by the U.S. Department of Energy, Office of Science, Basic Energy Sciences, Materials Sciences and Engineering Division. Use of electron microscopy at the Center for Nanoscale, an Office of Science user facility, was supported by the U.S. Department of Energy, Office of Science, Office of Basic Energy Sciences, under Contract No. DE-AC02-06CH11357. Band-structure calculations done at Nanjing University (by Y.D. and X.W.) are supported by the National Natural Science Foundation of China (Grants No. 11374137 and No. 11525417).

[1] M. Z. Hasan and C. L. Kane, Rev. Mod. Phys. **82**, 3045 (2010).
[2] X. L. Qi and S. C. Zhang, Rev. Mod. Phys. **83**, 1057 (2011).
[3] X. Zhu, H. Lei, C. Petrovic, and Y. Zhang, Phys. Rev. B **86**, 024527 (2012).
[4] M. Sturza, F. Han, C. D. Malliakas, D. Y. Chung, H. Claus, and M. G. Kanatzidis, Phys. Rev. B **89**, 054512 (2014).
[5] S. K. Kushwaha, J. W. Krizan, J. Xiong, T. Klimczuk, Q. D. Gibson, T. Liang, N. P. Ong, and R. J. Cava, J. Phys.: Condens. Matter **26**, 212201 (2014).
[6] N. Haldolaarachchige, S. K. Kushwaha, Q. Gibson, and R. J. Cava, Supercond. Sci. Tech. **27**, 105001 (2014).
[7] Z. K. Liu, B. Zhou, Y. Zhang, Z. J. Wang, H. M. Weng, D. Prabhakaran, S. K. Mo, Z. X. Shen, Z. Fang, and X. Dai, Science **343**, 864 (2014).
[8] S. Y. Xu, C. Liu, S. K. Kushwaha, R. Sankar, J. W. Krizan, I. Belopolski, M. Neupane, G. Bian, N. Alidoust, and T. R. Chang, Science **347**, 294 (2015).
[9] Z. Wang, Y. Sun, X.-Q. Chen, C. Franchini, G. Xu, H. Weng, X. Dai, and Z. Fang, Phys. Rev. B **85**, 195320 (2012).
[10] J. Park, G. Lee, F. Wolff-Fabris, Y. Y. Koh, M. J. Eom, Y. K. Kim, M. A. Farhan, Y. J. Jo, C. Kim, J. H. Shim, and J. S. Kim, Phys. Rev. Lett. **107**, 126402 (2011).
[11] J. K. Wang, L. L. Zhao, Q. Yin, G. Kotliar, M. S. Kim, M. C. Aronson, and E. Morosan, Phys. Rev. B **84**, 064428 (2011).
[12] K. Wang, D. Graf, H. Lei, S. W. Tozer, and C. Petrovic, Phys. Rev. B **84**, 220401(R) (2011).
[13] K. Wang, D. Graf, L. Wang, H. Lei, S. W. Tozer, and C. Petrovic, Phys. Rev. B **85**, 041101(R) (2012).
[14] L. Li, K. Wang, D. Graf, L. Wang, A. Wang, and C. Petrovic, Phys. Rev. B **93**, 115141 (2016).
[15] K. Wang, D. Graf, and C. Petrovic, Phys. Rev. B **87**, 235101 (2013).
[16] M. Sakano, K. Okawa, M. Kanou, H. Sanjo, T. Okuda, T. Sasagawa, and K. Ishizaka, Nat. Commun. **6**, 8595 (2015).
[17] Y. Nakajima, R. Hu, K. Kirshenbaum, A. Hughes, P. Syers, X. Wang, K. Wang, R. Wang, S. R. Saha, D. Pratt, J. W. Lynn, and J. Paglione, Sci. Adv. **1**, e1500242 (2015).
[18] F. F. Tafti, Q. Gibson, S. Kushwaha, J. W. Krizan, N. Haldolaarachchige, and R. J. Cava, Proc. Natl. Acad. Sci. USA **113**, E3475 (2016).
[19] S. Sun, Q. Wang, P.-J. Guo, K. Liu, and H. Lei, New J. Phys. **18**, 082002 (2016).
[20] N. Kumar, C. Shekhar, S.-C. Wu, I. Leermakers, O. Young, U. Zeitler, B. Yan, and C. Felser, Phys. Rev. B **93**, 241106(R) (2016).
[21] U. Schwarz, S. Tencé, O. Janson, C. Koz, C. Krellner, U. Burkhardt, H. Rosner, F. Steglich, and Y. Grin, Angew. Chem. Int. Ed. **52**, 9853 (2013).
[22] S. M. Clarke, J. P. Walsh, M. Amsler, C. D. Malliakas, T. Yu, S. Goedecker, Y. Wang, C. Wolverton, and D. E. Freedman, Angew. Chem. Int. Ed. **55**, 13446 (2016).
[23] F. Han, C. D. Malliakas, C. C. Stoumpos, M. Sturza, H. Claus, D. Y. Chung, and M. G. Kanatzidis, Phys. Rev. B **88**, 144511 (2013).
[24] R. Retzlaff, A. Buckow, P. Komissinskiy, S. Ray, S. Schmidt, H. Mühlig, F. Schmidl, P. Seidel, J. Kurian, and L. Alff, Phys. Rev. B **91**, 104519 (2015).
[25] F. Han, X. Wan, D. Phelan, C. C. Stoumpos, M. Sturza, C. D. Malliakas, Q. Li, T.-H. Han, Q. Zhao, D. Y. Chung, and M. G. Kanatzidis, Phys. Rev. B **92**, 045112 (2015).
[26] X. Lin, W. E. Straszheim, S. L. Bud'ko, and P. C. Canfield, J. Alloys Compd. **554**, 304 (2013).
[27] E. M. Seibel, W. Xie, Q. D. Gibson, and R. J. Cava, J. Solid State Chem. **230**, 318 (2015).
[28] C. B. R. Jesus, M. M. Piva, P. F. S. Rosa, C. Adriano, Z. Fisk, and P. G. Pagliuso, Phys. Proc. **75**, 618 (2015).
[29] J. P. Walsh, S. M. Clarke, Y. Meng, S. D. Jacobsen, and D. E. Freedman, ACS Cent. Sci. **2**, 867 (2016).
[30] A. Ovchinnikov and S. Bobev, Eur. J. Inorg. Chem. **2018**, 1266 (2018).
[31] E. Zintl, Angew. Chem. **52**, 1 (1939).
[32] A. K. Misra, Metall. Trans. A **22**, 715 (1991).
[33] S. Amano, D. Bogdanovski, H. Yamane, M. Terauchi, and R. Dronskowski, Angew. Chem., Int. Ed. **55**, 1652 (2016).
[34] See Supplemental Material at http://link.aps.org/supplemental/10.1103/PhysRevMaterials.3.105001 for SEM picture and

element analysis, x-ray crystallographic data (CIF), tables for detailed structure parameters, detailed magnetic susceptibility data from two different crystals, and resistivity data from another crystal.
[35] C. Stoe, Stoe & Cie, Darmstadt, Germany (2002).
[36] G. M. Sheldrick, Acta Cryst. A **64**, 112 (2008).
[37] G. Kresse and J. Hafner, Phys. Rev. B **48**, 13115 (1993).
[38] G. Kresse and D. Joubert, Phys. Rev. B **59**, 1758 (1999).
[39] J. P. Perdew, K. Burke, and M. Ernzerhof, Phys. Rev. Lett. **77**, 3865 (1996).
[40] D. Koelling and B. Harmon, J. Phys. C **10**, 3107 (1977).
[41] H. Bie and A. Mar, J. Solid State Chem. **182**, 3131 (2009).
[42] T. A. Strobel, K. C. Hester, E. D. Sloan, and C. A. Koh, J. Am. Chem. Soc. **129**, 9544 (2007).
[43] H. Zhang, H. Borrmann, N. Oeschler, C. Candolfi, W. Schnelle, M. Schmidt, U. Burkhardt, M. Baitinger, J. T. Zhao, and Y. Grin, Inorg. Chem. **50**, 1250 (2011).
[44] B. Fåk, E. Kermarrec, L. Messio, B. Bernu, C. Lhuillier, F. Bert, P. Mendels, B. Koteswararao, F. Bouquet, J. Ollivier, A. Hillier, A. Amato, R. H. Colman, and A. S. Wills, Phys. Rev. Lett. **109**, 037208 (2012).
[45] G. M. Zhang, Y. H. Su, Z. Y. Lu, Z. Y. Weng, D. H. Lee, and T. Xiang, Europhys. Lett. **86**, 37006 (2009).
[46] H. R. Naren, A. Thamizhavel, A. K. Nigam, and S. Ramakrishnan, Phys. Rev. Lett. **100**, 026404 (2008).
[47] C. Strack, C. Akinci, V. Pashchenko, B. Wolf, E. Uhrig, W. Assmus, M. Lang, J. Schreuer, L. Wiehl, J. A. Schlueter, J. Wosnitza, D. Schweitzer, J. Müller, and J. Wykhoff, Phys. Rev. B **72**, 054511 (2005).
[48] C. Urano, M. Nohara, S. Kondo, F. Sakai, H. Takagi, T. Shiraki, and T. Okubo, Phys. Rev. Lett. **85**, 1052 (2000).
[49] Q. Li, B. T. Liu, Y. F. Hu, J. Chen, H. Gao, L. Shan, H. H. Wen, A. V. Pogrebnyakov, J. M. Redwing, and X. X. Xi, Phys. Rev. Lett. **96**, 167003 (2006).
[50] H. Yang, Y. Liu, C. Zhuang, J. Shi, Y. Yao, S. Massidda, M. Monni, Y. Jia, X. Xi, Q. Li, Z.-K. Liu, Q. Feng, and H.-H. Wen, Phys. Rev. Lett. **101**, 067001 (2008).
[51] P. A. Lee and T. V. Ramakrishnan, Rev. Mod. Phys. **57**, 287 (1985).
[52] K. Kadowaki and S. Woods, Solid State Commun. **58**, 507 (1986).
[53] M. Rice, Phys. Rev. Lett. **20**, 1439 (1968).
[54] S. Y. Li, L. Taillefer, D. G. Hawthorn, M. A. Tanatar, J. Paglione, M. Sutherland, R. W. Hill, C. H. Wang, and X. H. Chen, Phys. Rev. Lett. **93**, 056401 (2004).
[55] T. Park, V. A. Sidorov, J. L. Sarrao, and J. D. Thompson, Phys. Rev. Lett. **96**, 046405 (2006).
[56] A. Jacko, J. Fjærestad, and B. Powell, Nat. Phys. **5**, 422 (2009).
[57] E. C. Stoner, Proc. R. Soc. A **154**, 656 (1936).